Journal of Materials Chemistry A

ROYAL SOCIETY OF CHEMISTRY

PAPER

View Article Online
View Journal

Cite this: DOI: 10.1039/d5ta10269c

Residual oxygen-driven p–n conversion and thermoelectric properties in CrN films

Yi Shuang, *[ab] Yuta Saito, [ac] Shogo Hatayama,[d] Mihyeon Kim,[a] Paul Fons [e] and Yuji Sutou *[ab]

Transition metal nitrides such as CrN are promising for thermoelectric applications due to their high stability and tunable electronic properties, yet they have been largely limited to n-type conduction, restricting device design. Here, we report the successful synthesis of p-type CrN films *via* controlled residual oxygen incorporation during RF magnetron sputtering regulated through N_2 gas flow adjustment, without introducing any additional oxygen source. A low N_2 gas flow rate (f_{N_2}) produces N-deficient $CrN_{1-\delta}$(O) films with n-type conduction dominated by nitrogen vacancies, while higher f_{N_2} (≥4 sccm) stabilizes Cr vacancies in over-stoichiometric $Cr_{1-\delta}N$(O) films, resulting in p-type hole conduction. Cr K-edge X-ray absorption fine structure (XAFS) reveals Cr–Cr bond elongation, reduced coordination, and enhanced Cr3d–O/N2p hybridization, indicative of localized hole states. Temperature-dependent transport measurements confirm the mechanisms, leading to a room-temperature power factor (PF) up to 0.105 mW m^{-1} K^{-2} (n-type) and 0.053 mW m^{-1} K^{-2} (p-type). The structural similarity between the n- and p-type films enables the creation of p–n homojunctions, highlighting a straightforward route for CrN-based thermoelectric devices.

Received 16th December 2025
Accepted 19th February 2026

DOI: 10.1039/d5ta10269c

rsc.li/materials-a

Introduction

Thermoelectric (TE) materials have emerged as key enablers for sustainable energy technologies, as they can directly convert waste heat into electrical energy without any moving parts or greenhouse emissions.[1] The energy conversion efficiency of a thermoelectric material is characterized by the dimensionless figure of merit, $ZT = S^2\sigma T/\kappa$, where S denotes the Seebeck coefficient, σ the electrical conductivity, and κ the thermal conductivity.[2,3] A high ZT thus requires the simultaneous enhancement of the power factor PF ($S^2\sigma$) and the suppression of heat transport. In the past few decades, extensive efforts have been devoted to improving bulk TE materials such as Bi_2Te_3, PbTe, and SnSe.[4] While these compounds have demonstrated outstanding ZT values near or above unity, their practical applications are constrained by scarcity, toxicity, or poor thermal and chemical stability, particularly at elevated temperatures. Recently, thin film thermoelectric devices have drawn growing interest due to their versatility in microelectronic integration and localized energy harvesting. Film configurations offer additional advantages such as microstructural engineering, strain modulation, and controlled carrier transport across nanoscale interfaces.[5] These properties make TE films attractive for emerging applications, including flexible temperature sensors,[6] microscale power generation applications[7] and on-chip energy harvesting devices.[8] Nevertheless, most conventional telluride-based TE films are chemically unstable, corrode easily, and degrade under thermal cycling, severely limiting their operational reliability at high temperatures.[9,10]

In this context, transition-metal nitrides (TMNs) and rare-earth nitrides (RENs) have been identified as promising candidates for robust thermoelectric films.[11–14] They possess high mechanical strength, excellent oxidation and corrosion resistance, moderate thermal conductivity, and a broad tunability in electrical transport properties. Among TMNs, chromium nitride (CrN) stands out as an n-type semiconductor with intriguing electronic and thermal characteristics. CrN exhibits relatively low resistivity together with a large Seebeck coefficient around 120 μV K^{-1}, resulting in a competitive power factor.[15,16] Furthermore, the high melting point and chemical inertness of CrN enable stable operation in harsh thermal environments, making it suitable for high-temperature TE applications.[17] The n-type conduction in CrN mainly originates from nitrogen

[a]Department of Material Science, Graduate School of Engineering, Tohoku University, 6-6-11, Aoba-yama, Aoba-ku, Sendai 980-8579, Japan. E-mail: shuang.yi.e3@tohoku.ac.jp; yuji.suto.b5@tohoku.ac.jp

[b]WPI Advanced Institute for Materials Research, Tohoku University, 2-1-1 Katahira, Aoba-ku, Sendai 980-8577, Japan

[c]Research Center for Green X-Tech, Tohoku University, 6-6-11, Aoba-yama, Aoba-ku, Sendai 980-8579, Japan

[d]Semiconductor Frontier Research Center, National Institute of Advanced Industrial Science and Technology (AIST), Tsukuba, 305-8568, Japan

[e]Department of Electronics and Electrical Engineering, Faculty of Science and Technology, Keio University, 3-14-1 Hiyoshi, Kohoku-ku, Yokohama, Kanagawa 223-8522, Japan

vacancies within its rocksalt structure, which provide donor-like states near the conduction band.[18] In addition, the intrinsic lattice instabilities of the rocksalt CrN phase contribute to a suppressed lattice thermal conductivity, a beneficial feature for thermoelectric performance.[15,19] Given the intrinsic low thermal conductivity of CrN, enhancing its *ZT* primarily relies on increasing the power factor through modulation of carrier concentration and carrier scattering mechanisms. The narrow bandgap in the range of 0–0.7 eV and high defect tolerance of CrN allow its electrical properties to be tuned from metallic to semiconducting regimes through compositional control and defect engineering.[16,20–23] However, for practical TE module design, both n- and p-type materials are essential. Ideally, these two components should possess similar crystal structures, thermal expansion coefficients, and mechanical properties to minimize interfacial strain and chemical interdiffusion.[24,25] One straightforward strategy is to achieve both n- and p-type conduction in a single material system. In this regard, p-type conduction in CrN has been reported to occur through metal-site substitutional doping. For example, alloying CrN with aluminium has been shown to induce a transition from n-type to p-type conduction, which was initially attributed to the substitution of Al for Cr and the associated modification of the electronic structure.[26] More recently, Mg-doped CrN has also been demonstrated to exhibit p-type behaviour. Density functional theory (DFT) calculations revealed that Mg substitution on the Cr site shifts the electronic bands upward such that the Fermi level enters the valence band, thereby inducing hole carriers.[27] These studies indicate that p-type transport in CrN can be achieved through appropriate substitutional metal doping *via* intrinsic band-structure modification.

Beyond intentional substitutional doping, subsequent studies have revealed that carrier polarity in CrN is highly sensitive to deviations from stoichiometry and native defect chemistry. In particular, Le Febvrier *et al.* demonstrated that the n–p type transition in CrN is primarily governed by the overall anion/cation ratio and the formation of Cr vacancies under nitrogen-rich conditions.[28] Their combined experimental and theoretical analysis showed that p-type conduction emerges when metal-site vacancies become dominant, while oxygen contamination at the 1–2% level mainly shifts the apparent transition point away from the ideal stoichiometric limit. Although theory predicts the transition to occur at zero deviation from stoichiometry, experimentally observed switching at $CrN_{1+\delta}$ with $\delta \approx -0.03$ highlights the strong sensitivity of carrier polarity to subtle changes in defect chemistry. Within this framework, oxygen incorporation should be considered as an important compositional factor that influences defect equilibria in TMN thin films, rather than as a direct acceptor itself. In reactive sputtering processes, oxygen contamination is difficult to control: even a slight partial pressure of oxygen, such as 3.0×10^{-3} Pa relative to a working pressure of 1.0 Pa, almost 40 at% oxygen can be incorporated into the growing TiN film.[29] Depending on the concentration, oxygen atoms will substitute for nitrogen sites or occupy interstitial positions, thereby acting as donors or acceptors and strongly affecting carrier polarity and mobility. Exploiting this unavoidable oxygen incorporation, rather than eliminating it, should provide a new approach for tuning the transport properties in, especially, semiconducting nitride films.

In this study, we demonstrate an oxygen-driven n–p conversion in CrN films achieved without any external oxygen source. Instead, we utilize the residual oxygen naturally present in the sputtering chamber and reproducibly control its incorporation by fixing the chamber base pressure at 10^{-5} Pa and simply adjusting the nitrogen gas flow rate (f_{N_2}) and the working pressure during radio-frequency (RF) magnetron sputtering. This straightforward yet highly effective approach enables accurate control of oxygen content, from 6.8 to 12.4 at% by just varying f_{N_2} from 2 to 8 sccm, and consequently, leading to a transition of CrN from n- to p-type conduction. The structural, electrical, and thermoelectric characteristics of the resulting CrN(O) (hereafter, the oxygen-incorporated CrN films are referred to as CrN(O) for simplicity) films were comprehensively investigated, revealing a strong correlation between oxygen incorporation and charge transport. This work provides a simple, cost-effective, and large-area-compatible strategy to tune carrier polarity in transition-metal nitrides, offering new insights into defect-mediated thermoelectric design.

Experimental

Preparation of CrN(O) films

CrN(O) films were deposited on Si/SiO_2 (100 nm) or quartz substrates by RF magnetron reactive sputtering of Cr (99.99%) pure target at room temperature (R.T.) in an Ar (99.999 vol%)/N_2 (99.999 vol%) atmosphere. The RF power of Cr was fixed at 50 W. The Ar gas flow rate was fixed at 15 sccm and the N_2 gas flow rate (f_{N_2}) varied from 0 to 10 sccm. The base pressure of the sputtering chamber was fixed at approximately 10^{-5} Pa. The working pressure during sputtering was around 0.34 Pa without flowing N_2 gas, and increased up to 0.54 Pa when the f_{N_2} flow was set to 10 sccm. The film thickness was measured by Atomic Force Microscopy (AFM).

Characterization of CrN(O) films

The composition of the films deposited at f_{N_2} values of 2, 6, and 8 sccm was determined by Rutherford backscattering (RBS, Pelletron 3SDH, National Electrostatics Corporation) using 2300 keV He ions at a scattering angle of 160 and 104°. The films for RBS measurements were deposited on Si/SiO_2 (100 nm) substrates with a thickness of 30 nm. To prevent surface oxidation, a 5 nm Cr cap layer was *in situ* deposited in the same sputtering chamber. The resulting compositional depth profiles from the surface to the substrate are shown in Fig. 1(a). It can be observed that, even with the 5 nm Cr cap, slight oxidation occurs near the interface between the CrN(O) film and the cap; however, the composition becomes uniform at greater depths, indicating the intrinsic presence of a small amount of oxygen in the CrN(O) films during sputtering. The elemental compositions were taken from the flat region of the depth profiles and are summarized in Table 1. A small amount of oxygen was confirmed in all films, and the oxygen content increased with

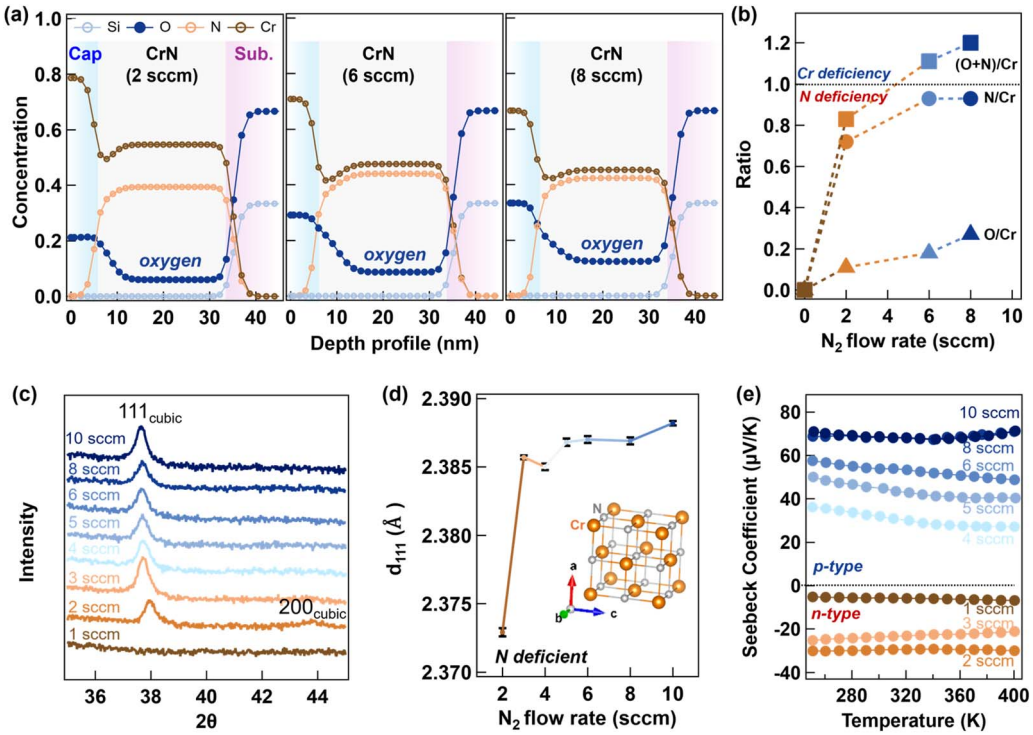

Fig. 1 (a) Concentration depth profile of Si, O, Cr, and N in CrN(O) films deposited at an f_{N_2} of 2, 6, and 8 sccm measured by RBS. (b) The atomic ratio of O/Cr, N/Cr and (O + N)/Cr calculated from RBS results taken from the uniform part of the depth profile. (c) XRD patterns, (d) $d_{(111)}$ and (e) temperature dependence of the Seebeck coefficient of the CrN(O) films at various f_{N_2}.

Table 1 Composition of the CrN(O) films determined by RBS

f_{N_2} (sccm)	Cr (at.%)	N (at.%)	O (at.%)	Working pressure (Pa)
2	54.7	39.3	6.0	0.38
6	47.5	43.9	8.6	0.46
8	45.3	42.3	12.4	0.50

increasing f_{N_2} and the associated working pressure. Since ultra-high purity argon (G1, O_2 < 0.1 vol. ppm) or nitrogen (G1, O_2 < 0.1 vol. ppm) gas was used, the oxygen incorporation discussed in this work arises from unavoidable residual oxygen in the sputtering system and is controlled indirectly through process parameters rather than by intentional oxygen dosing.

The crystal structures of the as-deposited CrN(O) films were investigated by X-ray diffraction (XRD, Rigaku; Ultima IV). The diffraction patterns were obtained in the 2θ range from 35° to 50° with Cu Kα radiation. Quartz substrates were used for XRD measurements. The cross-sectional microstructure of the CrN(O) films were observed using a field emission transmission electron microscope (FE-TEM, HF-2000EDX; Hitachi) at an accelerating voltage of 200 kV. TEM samples of the CrN(O) films were thinned using ion milling (PIPS; Gatan). X-ray photoelectron spectroscopy (XPS, Thermo VG; Theta Probe) was performed to analyze the chemical bonding state of elements in the CrN(O) films. Ar ion etching for 60 min with a 1 kV ion gun was carried out to remove the surface oxidation layer before the XPS measurements. All energies were calibrated using the C 1s peak at 285.0 eV. The films for TEM and XPS measurements were deposited on Si/SiO_2 (100 nm) substrates. X-ray absorption fine structure (XAFS) measurements were carried out at beamline BL01B1 at SPring-8 of the Japan Synchrotron Radiation Research Institute (JASRI). Cr K-edge spectra were recorded in fluorescence mode 100-nm-thick CrN(O) films at an f_{N_2} of 2, 4 and 6 sccm were deposited onto quartz substrates for the measurements. A 5-nm-thick SiO_2 layer was deposited on the surface of the CrN(O) films to prevent surface oxidation. The XAFS data obtained were analyzed using Athena and Artemis software.[30] The electrical properties of the film were evaluated by Hall-effect measurements (Toyo Corp.; ResiTest 8400). The temperature dependence of the resistivity of the CrN(O) films was measured by the van der Pauw method in a He atmosphere. The temperature range was set to be 250–400 K with a step of 10 K. AC Hall measurements (Toyo Corp.; ResiTest 8400) were carried out to measure the Hall properties at RT in the same chamber as that used for the resistivity measurements. The Seebeck coefficient S was measured (Toyo Corp.; ResiTest 8300) over the temperature range of 260–400 K. The above electrical characterization studies were carried out on uncapped CrN films immediately after film growth. Insulating quartz substrates were selected to avoid any unwanted parallel conduction paths during the electrical measurements. The thermal conductivity of selected CrN(O) thin films was measured using the time-domain thermoreflectance (TDTR) technique (PicoTR system; NETZSCH).

First-principles calculations

The first-principles calculations of oxygen incorporating CrN films were carried out using Density Functional Theory (DFT) calculations. These calculations were conducted using the Vienna *Ab initio* Simulation Package (VASP) and projector augmented plane wave (PAW) pseudopotentials, with the Perdew–Burke–Ernzerhof (PBE) generalized gradient approximation (GGA) for handling exchange and correlation effects. Several possible crystal model candidates with different defect states were considered using $3 \times 3 \times 3$ supercells of cubic CrN ($Fm\bar{3}m$). Each system was fully relaxed. The plane-wave cut-off energy was set at 400 eV.

Results and discussion

Structural analysis

Fig. 1(b) shows the atomic ratio of O/Cr, N/Cr and (O + N)/Cr calculated from the RBS results for the CrN(O) films. The CrN(O) film deposited at $f_{N_2} = 2$ sccm was off-stoichiometric with a N/Cr ratio less than 1 and an oxygen content of around 6.0 at% ($CrN_{0.72}O_{0.11}$). Since the Ar flow rate was fixed at 15 sccm, the increase in f_{N_2} increased the working pressure, leading to a higher oxygen partial pressure and consequently leading to increased oxygen content in the films. Similar behavior was observed in zinc oxy-nitride films, where the oxygen concentration was found to increase with working pressure.[31] For f_{N_2} values above 6 sccm, the N/Cr ratio approached 1, but the total N + O concentration exceeded the Cr concentration, indicating Cr-deficiency. Specifically, the CrN(O) films deposited at $f_{N_2} = 6$ and 8 sccm contained ~8.6 at% O ($CrN_{0.93}O_{0.18}$), and ~12.4 at% O ($CrN_{0.93}O_{0.27}$), respectively. Fig. 1(c) shows XRD patterns of the as-grown films at R.T., illustrating the phase evolution as a function of f_{N_2}. At $f_{N_2} = 1$ sccm, the reflection peaks are very weak, suggesting a very fine microstructure and the coexistence of multiple minor phases such as Cr or Cr_2N in addition to CrN. When f_{N_2} exceeds 2 sccm, the NaCl-type cubic CrN phase begins to form. At this stage, 111_{cubic} and 200_{cubic} reflections appear at relatively higher angles, indicating a reduced lattice constant due to insufficient nitrogen content and the presence of numerous nitrogen vacancies. For $f_{N_2} \geqq 3$ sccm, the NaCl-type cubic phase exhibits a pronounced (111) preferred orientation parallel to the substrate, with the 111_{cubic} peak gradually shifting to lower angles with increasing f_{N_2}, reflecting lattice expansion as nitrogen atoms occupy previously vacant sites. The peak positions and intensities remain essentially unchanged for $f_{N_2} \geqq 3$ sccm, suggesting that the nitrogen content approaches saturation and stoichiometric CrN is formed. The *d*-spacing of the (111) planes plotted in Fig. 1(d) was calculated from the 111 peak positions, with the peak fitting details shown in Fig. S1. The results show a marked increase in the f_{N_2} region from 2 to 3 sccm, further supporting the hypothesis of a nitrogen-deficient state of the CrN lattice in the low f_{N_2} region, consistent with the RBS results. No secondary phases were detected, indicating that the small amount of oxygen incorporated into the films does not significantly alter the crystal structure.

Fig. 1(e) shows the temperature dependence of the Seebeck coefficient for CrN(O) films deposited under different f_{N_2} conditions. The films deposited with $f_{N_2} \leqq 3$ sccm exhibit n-type semiconductor behavior with a negative Seebeck coefficient, consistent with previous reports.[15,32] The Seebeck coefficient ranges from approximately −7 to −30 μV K^{-1} at 250 K and remains nearly constant with increasing temperature, the values of which are significantly smaller than the typical stoichiometric CrN value of around −120 μV K^{-1} at 300 K. The reduced absolute value can be attributed to the higher carrier concentration in nitrogen-deficient CrN films, as described by the Mott–Boltzmann relation:

$$S = \frac{8\pi^2 {k_B}^2 T}{3eh^2} m^* \left(\frac{\pi}{3n_i}\right)^{\frac{2}{3}} \quad (1)$$

where k_B is the Boltzmann constant, h the Planck's constant, T the temperature, m^* the effective mass, e the elementary charge and n_i the carrier concentration. As indicated by this equation, the Seebeck coefficient is inversely proportional to the carrier concentration and directly proportional to the effective mass, which will be discussed in detail later. In contrast, films deposited at $f_{N_2} \geqq 4$ sccm exhibited a positive Seebeck coefficient, indicating p-type conduction. This result strongly suggests that the residual oxygen naturally present in the sputtering chamber, modulated by f_{N_2}, can effectively be used to tune the conduction type of CrN(O) films. Interestingly, this p-type behavior induced by oxygen incorporation differs from that in previous studies. In early reports, oxygen doping was shown to suppress the Seebeck coefficient in n-type CrN films.[33,34] This effect is primarily attributed to electron doping: when oxygen substitutes for nitrogen in already n-type CrN, oxygen incorporation introduces additional electrons, thereby increasing the electron carrier concentration and reducing the Seebeck coefficient. Moreover, McGahay *et al.* reported that, substituting nitrogen with oxygen on anion sites of CrN results in n-type doping which, however, is partially compensated for by the formation of negatively charged Cr vacancies acting as acceptors.[35] Febvrier *et al.* further demonstrated that the carrier type in CrN is governed by the Cr/N ratio, and that even a small amount of oxygen incorporation can shift the apparent n–p transition away from the ideal stoichiometric limit.[28] In this work, however, oxygen incorporation led to both conduction-type inversion and an enhancement in the Seebeck coefficient.

We further performed cross-sectional TEM of N-deficient and Cr-deficient CrN(O) thin films to investigate possible microstructure changes. Fig. 2(a) and (c) show bright field cross-sectional TEM images of a CrN(O) film deposited at a f_{N_2} of 2 sccm ($CrN_{0.72}O_{0.11}$, n-type) and 6 sccm ($CrN_{0.93}O_{0.18}$, p-type), indicating that both films exhibit a columnar-like grain microstructure. The surfaces of both films are relatively smooth. Fig. 2(b) and (e) show selected area electron diffraction (SAED) patterns of the films, showing a ring pattern typical of the polycrystalline phase. Both N-deficient and Cr-deficient CrN(O) films were determined to be a single NaCl-cubic CrN phase. From the lattice spacing analysis of each crystalline plane, it is

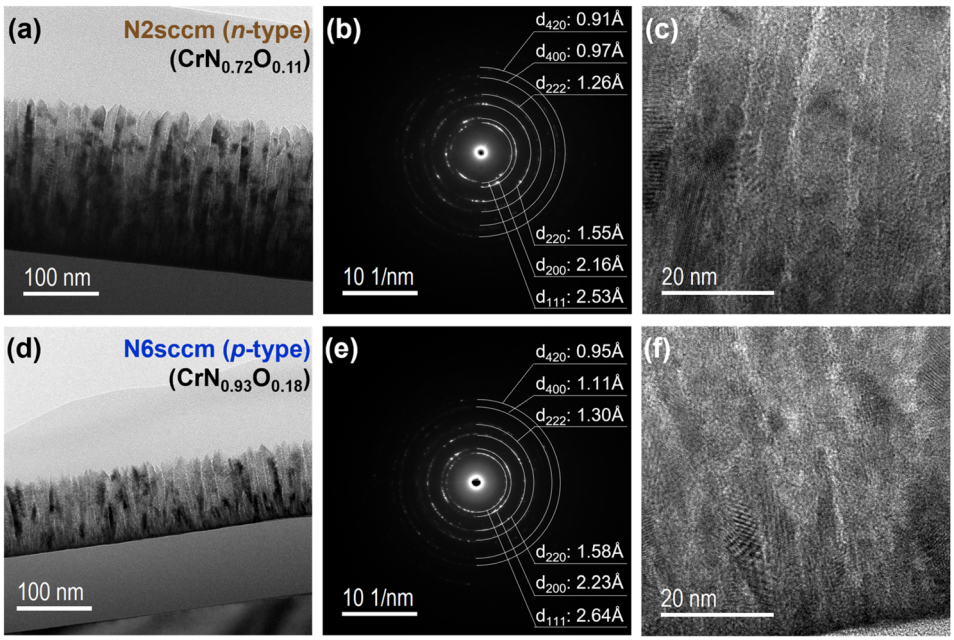

Fig. 2 Cross-sectional TEM image of a CrN(O) film deposited at a f_{N_2} of (a) 2 sccm ($CrN_{0.72}O_{0.11}$) and (d) 6 sccm ($CrN_{0.93}O_{0.18}$). Diffraction patterns and indexing of the (b) $CrN_{0.72}O_{0.11}$ and (e) $CrN_{0.93}O_{0.18}$ films. STEM images of the (c) $CrN_{0.72}O_{0.11}$ and (f) $CrN_{0.93}O_{0.18}$ films.

evident that upon further increases in f_{N_2}, nitrogen atoms gradually occupy nitrogen-vacancy sites, resulting in an overall lattice expansion. This trend is consistent with the XRD results, where the diffraction peaks systematically shift toward lower 2θ values. In addition, as shown in Fig. 2(c) and (f), high-resolution Scanning Transmission Electron Microscopy (STEM) images reveal clear lattice fringes, further confirming that both n- and p-type CrN(O) films possess well-crystallized microstructures despite compositional differences. The chemical bonding states of both films were also characterized by XPS with the results shown in Fig. S2. It was found that both Cr $2p_{3/2}$ and Cr $2p_{1/2}$ peaks could be separated into two peaks using Gaussian fitting for the $CrN_{0.93}O_{0.18}$ film. The peaks at 574.83 eV and 584.28 eV are identified as Cr^{3+} due to the presence of Cr–N bonds, while the peaks at higher energy of 576.43 eV and 586.35 eV can be regarded as oxidized peaks due to the stronger binding energy of Cr–O. The N 1s peak at 397.38 eV may indicate that the N is bonded with Cr atoms. The appearance of the O 1s peak even after the removal of the surface oxidation layer also suggests the existence of O atoms. However, no obvious peak shift can be found between n-type $CrN_{0.72}O_{0.11}$ and p-type $CrN_{0.93}O_{0.18}$ films. Since no significant changes in the crystal structure were observed upon oxygen incorporation by XRD, TEM and XPS, more sensitive tools were employed such as synchrotron XAFS spectroscopy to further investigate the local structural variations and defect configurations responsible for the observed p–n conversion.

Febvrier *et al.* showed that Cr vacancies introduce hole carriers and shift the Fermi level toward the valence band, giving rise to p-type conduction.[28] Our observation that films deposited at $f_{N_2} \geqq 4$ sccm exhibit p-type behavior is therefore plausibly explained by a high concentration of Cr vacancies in these Cr-deficient films. To directly probe this hypothesis, we examined the local coordination of Cr in films deposited at $f_{N_2} =$ 2, 4, and 6 sccm by Cr K-edge extended X-ray absorption fine structure (EXAFS). Fig. 3(a) displays the Fourier transform (FT) of the k^3-weighted χ (R) spectra (plotted *versus* the radial distance R). No secondary crystalline phases other than NaCl-type cubic CrN were detected in XRD, and the χ (R)-R spectra differed markedly from those of chromium oxides. Note that the distances shown in Fig. 3(a) are shorter than the crystallographic distances due to the presence of phase shifts. The phase shifts were accounted for in the fitting process. Accordingly, we assigned the first-nearest-neighbour peak to the Cr–N shell (nominal $R_{Cr-N} \sim 2.08$ Å, coordination number (CN) ~ 6) and the second-neighbour peak to the Cr–Cr shell (nominal $R_{Cr-Cr} \sim 2.95$ Å, CN ~ 12).[36] The Cr–O scattering path was not considered in the fitting, as its inclusion did not improve but instead degraded the fitting quality, consistent with our previous report.[37] With increasing f_{N_2}, the Cr–N peak position and intensity remain nearly unchanged, whereas the Cr–Cr peak intensity increased noticeably, suggesting a variation in Cr–Cr coordination. Because the EXAFS peak intensity is directly related to the CN, we quantitatively analysed these changes by fitting the χ (R) spectra in the R-space range of 1–3 Å, as shown in Fig. 3(a). The best fit was done for this plot within the k-range of 3–12 Å (Fig. 3(b)). The extracted local structural parameters are summarized in Fig. 3(c–e) and Table 2.

The fitted Cr–N coordination number remains near the theoretical value ($\sim$6) and shows only minor fluctuations with f_{N_2}, indicating that the local octahedral Cr–N environment is largely preserved (Fig. 3(d)). In contrast, the Cr–Cr coordination number systematically decreases with increasing f_{N_2}, reaching $\sim$8.8 at $f_{N_2} = 6$ sccm (from the ideal 12), which unambiguously

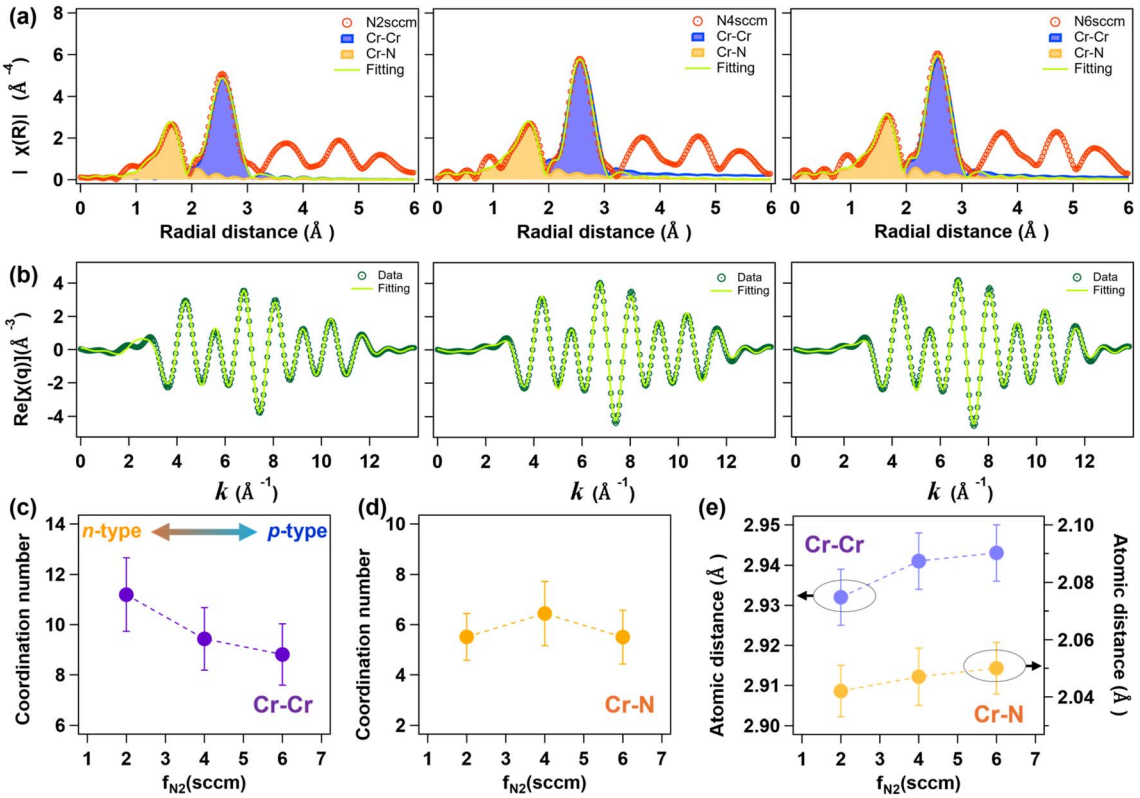

Fig. 3 (a) Fourier transformed EXAFS data at the Cr K-edge and fitting results for CrN(O) films deposited at an f_{N_2} of 2, 4, and 6 sccm. (b) Experimental and simulated back-Fourier transformed EXAFS spectra of the CrN(O) films deposited at an f_{N_2} of 2, 4, and 6 sccm. The simulated coordination number of (c) Cr–Cr and (d) Cr–N paths. (e) The atomic distances of Cr–Cr and Cr–N paths.

Table 2 Curve fitting results of Cr K-edge EXAFS in the CrN(O) films deposited at an f_{N_2} of 2, 4, and 6 sccm

f_{N_2} (sccm)	Path	Coordination number, CN	Atomic distance (Å), R	Debye–Waller factor, σ^2	Reduced, χ^2
2	Cr–Cr	11.19 ± 1.46	2.932 ± 0.007	0.008	80.69
	Cr–N	5.51 ± 0.93	2.042 ± 0.009	0.005	
4	Cr–Cr	9.43 ± 1.25	2.941 ± 0.007	0.008	81.32
	Cr–N	6.44 ± 1.28	2.047 ± 0.010	0.006	
6	Cr–Cr	8.81 ± 1.22	2.943 ± 0.007	0.007	62.09
	Cr–N	5.50 ± 1.07	2.050 ± 0.009	0.005	

indicates a significant concentration of Cr vacancies (Cr-site deficiency) in the high- f_{N_2} films (Fig. 3(c)). This result is consistent with our previous transmission-mode EXAFS study on films deposited under the same conditions (f_{N_2} = 6 sccm) on Al foil, which also evidenced reduced Cr–Cr coordination.[37] As the f_{N_2} increases, leading to oxygen incorporation, both Cr–N and Cr–Cr bond lengths slightly increase (Fig. 3(e)). We attribute this to substitutional oxygen on nitrogen sites (O_N), which is thermodynamically favoured over interstitial occupation. Substitutional O_N leads to local charge redistribution and lattice relaxation, producing slight increases in Cr–N and Cr–Cr bond lengths on the order of ~0.01–0.03 Å. These local structural changes are directly linked to the electronic structure and p-type conduction mechanism. In ideal CrN, three nonbonding 3d electrons remain localized around the Cr atom, resulting in limited intrinsic conductivity. The introduction of Cr vacancies decreases the electron occupation of the Cr 3d states at the vacant sites, generating localized hole states predominantly in the Cr 3d–N 2p hybridized bands, which act as p-type carriers. Oxygen substitution further modifies these states: due to its higher electronegativity, oxygen enhances Cr 3d–O 2p hybridization, altering the local electronic density and slightly raising the 3d energy levels, thereby stabilizing hole states and increasing their concentration. Simultaneously, the Cr–Cr and Cr–N bond elongation narrows the 3d bandwidth, enhancing electron localization and facilitating the formation and detection of additional unoccupied states.

Cr K-edge X-ray absorption near edge structure (XANES) confirms this picture, as the emergence of a new pre-edge peak (corresponding to the 1s → 3d transition) at around 5992 eV

indicates an increase in unoccupied 3d states corresponding to these localized holes. These unoccupied states directly reflect the presence of localized holes on Cr sites: the absence of electrons in the 3d orbitals allows 1s core electrons to be excited into these vacant states. Therefore, the pre-edge intensity provides a direct probe of the formation and concentration of Cr 3d holes induced by defects or oxygen substitution (Fig. 4).

Together, the EXAFS and XANES observations demonstrate that Cr vacancies and oxygen-induced local electronic structure modifications collectively generate hole carriers, providing a microscopic explanation for the observed p-type conduction in Cr-deficient, oxygen-incorporating CrN films.

Electrical transport analysis

We further investigated the thermoelectric properties. Fig. 5(a) summarizes the R.T. Seebeck coefficient of films deposited at various f_{N_2} as already shown in Fig. 1(e). Films deposited at low f_{N_2} (1–3 sccm) exhibit negative Seebeck coefficients, and all films deposited at f_{N_2} higher than 4 sccm display positive Seebeck coefficients with significantly larger absolute values. The Seebeck coefficient increases from 36.1 μV K^{-1} to 68.8 μV K^{-1} with increasing f_{N_2} from 4 to 8 sccm and saturates. In contrast to the n-type CrN films, where the Seebeck coefficient can be reasonably described by the Mott–Boltzmann expression (eqn (1)) derived under the assumption of the presence of itinerant electrons in a parabolic band, the p-type behavior observed here arises from vacancy-related, localized hole states associated with Cr vacancies. Since these holes are strongly localized, the concept of an effective mass is not strictly applicable. Accordingly, the enhancement of the Seebeck coefficient is better interpreted within the general Mott relation, which relates the Seebeck coefficient to the energy dependence of the electronic states near the Fermi level, rather than solely to the effective mass. This framework captures the qualitative effect of oxygen incorporation and vacancy stabilization on the electronic structure and is consistent with the observed increase in the Seebeck coefficient. Fig. 5(b) presents the R.T. resistivity as measured by the van der Pauw method. The resistivity increases sharply from 8.40×10^{-4} Ω cm to a maximum of 1.58×10^{-2} Ω cm in the f_{N_2} range below 5 sccm, followed by a slight decrease to 7.96×10^{-3} Ω cm for higher f_{N_2}. The corresponding power factor (PF $= S^2\sigma$), as shown in Fig. 5(c), reaches the maximum values of 0.105 mW m^{-1} K^{-2} in n-type $CrN_{0.72}O_{0.11}$ ($f_{N_2} = 2$ sccm) and 0.053 mW m^{-1} K^{-2} in p-type $CrN_{0.93}O_{0.27}$ ($f_{N_2} = 8$ sccm). These values are larger than those of some bulk CrN materials, such as n-type bulk CrN with PF values of around 0.03 mW m^{-1} K^{-2} according to ref. 26 and 0.02 mW m^{-1} K^{-2} from ref. 11 at R.T.; these values are a little bit lower than that of the reported highest n-type CrN films with a PF value of around 0.15 mW m^{-1} K^{-2} at R.T.[15] In addition, the PF value of the p-type $CrN_{0.93}O_{0.27}$ film at R.T. is comparable with that reported for a p-type $Cr_{0.96}Al_{0.04}N_{1.17}$ film which had a PF of 0.05 mW m^{-1} K^{-2} [26]. To further assess the thermoelectric performance, thermal conductivity measurements were performed on the representative n-type ($CrN_{0.72}O_{0.11}$) and p-type ($CrN_{0.93}O_{0.18}$) films exhibiting high PF values. The n-type CrN(O) film shows a thermal conductivity of approximately 2.7 W m^{-1} K^{-1}, consistent with previously reported values for sputtered n-type CrN thin films.[15] Upon oxygen incorporation and p-type conversion, the thermal conductivity decreased to approximately 1.8 W m^{-1} K^{-1}, suggesting enhanced phonon scattering induced by oxygen-related defects and cation vacancies. Based on the measured electrical and thermal transport properties, the R.T. *ZT* value of a n-type CrN(O) film is approximately 0.012, comparable to most as-deposited CrN thin films, though lower than values reported for epitaxial CrN films subjected to high-temperature annealing.[15,38] The R.T. *ZT* value of the p-type film was 0.006. To the best of our knowledge, the thermal conductivity and *ZT* values for p-type CrN thin films are reported here for the first time. This demonstrates that controlled oxygen incorporation and the engineering of Cr vacancies can effectively tune carrier type while maintaining competitive thermoelectric performance.

To understand the conduction mechanisms in detail, temperature-dependent resistivity, carrier concentration, and Hall mobility were measured from 250 to 400 K in the representative n-type CrN(O) ($CrN_{0.72}O_{0.11}$, $f_{N_2} = 2$ sccm) and p-type CrN(O) ($CrN_{0.93}O_{0.27}$, $f_{N_2} = 8$ sccm) films (Fig. S3(d–f)). Both films display a negative temperature coefficient of resistivity, confirming semiconducting behavior. The Hall-effect measurements reveal that, for the n-type CrN(O) film, the carrier concentration increased monotonically with temperature while the Hall mobility decreases gradually, indicating that conduction is dominated by thermally activated free electrons with mobility limited by lattice or impurity scattering. The large amount of N vacancies in the film results in a higher electron concentration of 9.59×10^{22} cm^{-3} compared to that of a typical stoichiometric CrN film (order of 10^{20} cm^{-3}), which may lead to a reduction of the Seebeck coefficient larger than that of bulk CrN as mentioned in eqn (1). In contrast, the p-type CrN(O) film exhibits nearly constant carrier concentration but increasing Hall mobility with temperature, consistent with conduction mediated by localized hole states formed near Cr vacancies and through Cr–O hybridized orbitals. The temperature-dependent

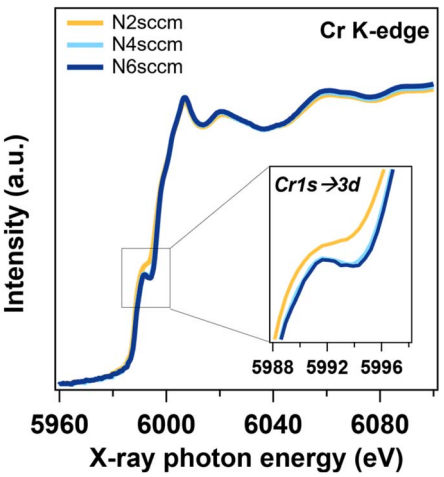

Fig. 4 XANES spectra at the K-edge of CrN(O) films at $f_{N_2} = 2$, 4, and 6 sccm.

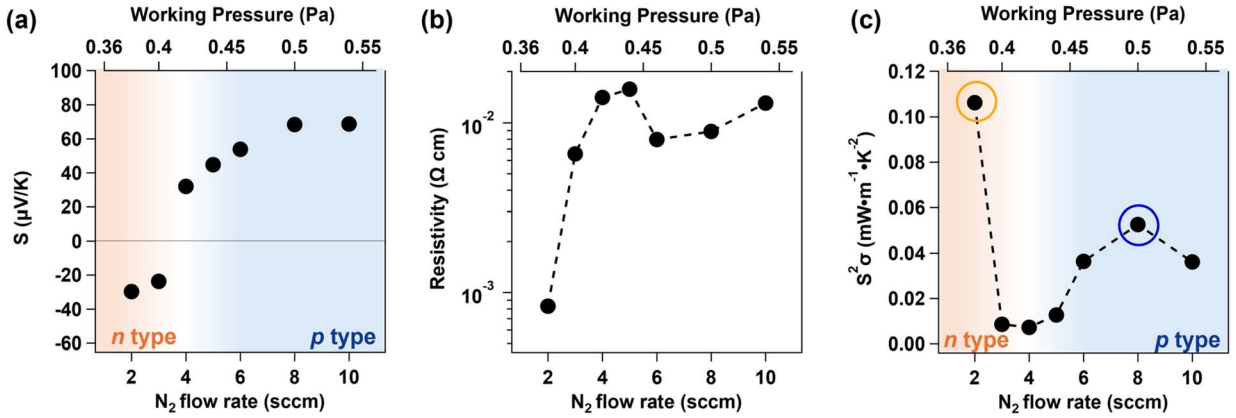

Fig. 5 (a) Seebeck coefficient, (b) resistivity and (c) power factor of the CrN(O) films at various N_2 gas flow rates, f_{N_2}, at R.T.

increase in mobility can be attributed to hopping conduction of these localized holes: as the temperature increases, thermal energy facilitates the hopping between neighboring localized states, enhancing mobility. The absolute mobility of these holes is much lower, by approximately two orders of magnitude, than that of the n-type electrons in CrN, reflecting the difference between narrow-band, localized hopping transport and wide-band, quasi-free electron conduction.

Further Hall-effect measurements at R.T. across the full f_{N_2} range (2–10 sccm, Fig. 6(a and b)) reveal an evolution of carrier type. Hall-effect measurements showed that films at f_{N_2} = 2–5 sccm exhibit n-type conduction, whereas those at f_{N_2} > 5 sccm exhibit p-type conduction. Notably, films at f_{N_2} = 4–5 sccm

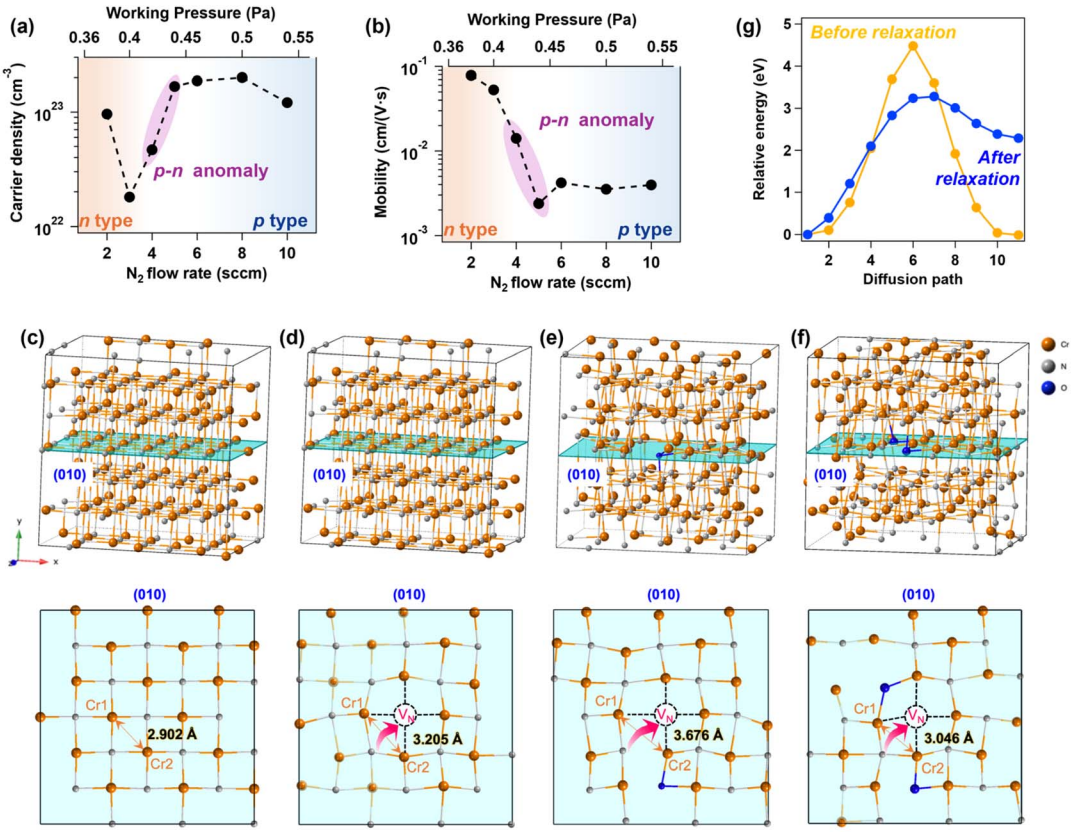

Fig. 6 (a) Carrier density and (b) mobility of the CrN(O) films deposited at various N_2 gas flow rates, f_{N_2}, at R.T. Relaxed 3 × 3 × 3 supercell of (c) CrN; (d) CrN with one N vacancy site; (e) CrN with one N vacancy site and one substituted O atom; (f) CrN with one N vacancy site and two substituted O atoms; the figures under the supercell are (010) planes chosen from the supercell near the N vacancies. (g) The barrier energy change of N atom as a function of the diffusion path.

exhibit a p–n anomaly: the Seebeck coefficient is positive, while Hall-effect measurements indicate n-type carriers. First-principles calculations provide a microscopic explanation. Alling *et al.* reported that CrN is paramagnetic with robust local magnetic moments on Cr atoms.[39] In the present study, first-principles calculations are employed to examine local structural relaxations around point defects. Since the calculations are not intended to describe electronic band structures or magnetic excitations, the focus on defect-induced lattice distortions is expected to capture the essential structural trends relevant to the experimental observations. In Fig. 6(c), we present a 3 × 3 × 3 supercell of cubic CrN ($Fm\bar{3}m$). To explore the nitrogen vacancy diffusion process in n-type CrN(O), we first introduced a nitrogen vacancy to create a path for nitrogen diffusion, as depicted in Fig. 6(d). Subsequently, we placed one or two oxygen atoms near the nitrogen vacancy, as shown in Fig. 6(e and f). Each structure underwent full relaxation, and we selected the (010) crystal plane for examination beneath the supercell. Upon relaxation of the supercell with a nitrogen vacancy (Fig. 6(d)), we observed that the Cr–Cr distance near the vacancy (Cr1–Cr2) increased, reducing the energy barrier for neighboring nitrogen atoms to diffuse into the vacancy (Fig. 6(g)). When one oxygen atom (low oxygen content, corresponding to $f_{N_2} \approx$ 3–5 sccm) was introduced near the nitrogen vacancy, as depicted in Fig. 6(e), the higher bonding energy of Cr–O caused the Cr atoms to be drawn towards the oxygen side, resulting in longer and weaker Cr–Cr bonds. The elongation of the Cr–Cr bonds softens the local lattice and lowers both the formation and migration barriers for nitrogen vacancies. Because nitrogen vacancies act as electron-donor defects in CrN, the presence of more mobile and easily ionized nitrogen vacancies increases the concentration of activated donor states, resulting in a relatively higher n-type carrier density CrN(O) ($f_{N_2} \approx$ 4–5 sccm). However, the concomitant lattice distortion significantly reduces carrier mobility. In this regime, high-mobility electrons dominate the Hall response, leading to n-type Hall measurements, while the newly formed localized hole states, which contribute strongly to the thermopower, yield a positive Seebeck coefficient. At higher oxygen concentrations (~2 O atoms, f_{N_2} > 5 sccm), the local formation of Cr–O bonds result in slightly shortened nearby Cr–Cr distances and suppression of long-range nitrogen-vacancy diffusion. At the same time, the increased oxygen content shifts the overall stoichiometry toward (N + O) > Cr, making charge compensation through the formation of Cr vacancies energetically more favorable than through nitrogen vacancies (Fig. 6(f)). This stabilizes the localized hole states, resulting in p-type conduction for both Seebeck and Hall-effect measurements. EXAFS and XANES corroborate this picture: Cr–Cr bond lengths increase with oxygen incorporation, coordination numbers decrease, and the Cr K-edge XANES pre-edge peak grows, confirming the formation of localized unoccupied 3d states. Temperature-dependent mobility trends further support the transport interpretation: n-type films are electron-dominated with mobility decreasing at higher temperatures, while p-type films exhibit activation-dominated hole transport *via* localized states. The correlation between microscopic defects, localized electronic states, and macroscopic transport properties illustrates that careful tuning of f_{N_2} (oxygen content) enables controlled carrier type and optimized thermoelectric performance in CrN(O) films.

Conclusions

In conclusion, p-type CrN(O) films have been successfully developed by incorporating residual oxygen impurities during RF magnetron sputtering through careful regulation of N_2 gas flow control. At low f_{N_2}, the N/Cr atomic ratio was less than 1, leading to N-deficient CrN(O) films in which nitrogen vacancies dominate, resulting in n-type conduction. As f_{N_2} is increased to over 4 sccm, the N/Cr ratio approached unity, but oxygen incorporation simultaneously occurred, producing over-stoichiometric CrN(O) films with a total (O + N)/Cr ratio greater than 1. In these films, Cr vacancies were generated and stabilized, giving rise to p-type hole conduction. The optimal compositions for thermoelectric performance were identified as $CrN_{0.72}O_{0.11}$ for n-type and $CrN_{0.93}O_{0.27}$ for p-type films, exhibiting the highest R.T. power factor values.

Structural and spectroscopic analyses revealed that both n- and p-type films possess similar NaCl-type cubic microstructures, with subtle variations in Cr–Cr bond lengths, local coordination, and Cr3d–O/N2p hybridization, which underpin the observed carrier type and transport properties. The coexistence of these n- and p-type films with comparable crystal structures provides a promising platform for the formation of p–n homojunctions, potentially enabling integrated thermoelectric devices with improved compatibility and efficiency. These findings demonstrate a straightforward and controllable strategy to achieve both n- and p-type CrN(O) films, linking defect engineering, oxygen incorporation, and carrier type control, and open new avenues for nitride film thermoelectric applications.

Conflicts of interest

There are no conflicts to declare.

Data availability

The data supporting the findings of this study are available within the article and from the corresponding author upon reasonable request.

Supplementary information (SI): Fig. S1–S3. See DOI: https://doi.org/10.1039/d5ta10269c.

Acknowledgements

This work was supported by JSPS KAKENHI (Grant No. 24K00915 and 21H05009), the Thermal & Electric Energy Technology Foundation (TEET) and the FY2023 Fusion Research Funds from WPI-AIMR, Tohoku University. The authors acknowledge financial support from the JST FOREST Program, Grant No. JPMJFR235T. This work was supported by the WAKASAPO program of the New Energy and Industrial

Technology Development Organization (NEDO), Japan. The authors thank Dr T. Miyazaki (Tohoku University, Japan) for his technical support with the TEM measurements.

Notes and references

1 F. J. Disalvo, *Science*, 1999, **285**, 703–706.
2 J. He and T. M. Tritt, *Science*, 2017, **357**, eaak9997.
3 G. J. Snyder and E. S. Toberer, *Nat. Mater.*, 2008, **7**, 105–114.
4 T. Deng, Z. Gao, Z. Li, P. Qiu, Z. Li, X. Yuan, C. Ming, T. R. Wei, L. Chen and X. Shi, *Science*, 2024, **386**, 1112–1117.
5 X. Chen, Z. Zhou, Y. H. Lin and C. Nan, *J. Materiomics*, 2020, **6**, 494–512.
6 C. Bianchi, J. Loureiro, P. Duarte, J. Marques, J. Figueira, I. Ropio and I. Ferreira, *Adv. Mater. Technol.*, 2016, **1**, 1600077.
7 N. S. Hudak and G. G. Amatucci, *J. Appl. Phys.*, 2008, **103**, 101301.
8 S. H. Choday, M. S. Lundstrom and K. Roy, *IEEE Trans. Compon., Packag., Manuf. Technol.*, 2013, **3**, 2059–2067.
9 P. Mannu, M. Palanisamy, G. Bangaru, S. Ramakrishnan, R. Meena, C. L. Dong and A. Kandasami, *Appl. Surf. Sci.*, 2020, **505**, 144115.
10 R. Lan, S. L. Otoo, P. Yuan, P. Wang, Y. Yuan and X. Jiang, *Appl. Surf. Sci.*, 2020, **507**, 145025.
11 C. X. Quintela, F. Rivadulla and J. M. Rivas, *Appl. Phys. Lett.*, 2009, **94**, 152103.
12 P. Eklund, S. Kerdsongpanya, B. Rn and A. Ab, *J. Mater. Chem. C*, 2016, **4**, 3905.
13 S. Kerdsongpanya, N. Van Nong, N. Pryds, A. Žukauskaite, J. Jensen, J. Birch, J. Lu, L. Hultman, G. Wingqvist and P. Eklund, *Appl. Phys. Lett.*, 2011, **99**, 232113.
14 A. Le Febvrier, N. Tureson, N. Stilkerich, G. Greczynski and P. Eklund, *J. Phys. D Appl. Phys.*, 2019, **52**, 035302.
15 C. X. Quintela, J. P. Podkaminer, M. N. Luckyanova, T. R. Paudel, E. L. Thies, D. A. Hillsberry, D. A. Tenne, E. Y. Tsymbal, G. Chen, C. Eom and F. Rivadulla, *Adv. Mater.*, 2015, **27**, 3032–3037.
16 M. A. Gharavi, S. Kerdsongpanya, S. Schmidt, F. Eriksson, N. V. Nong, J. Lu, B. Balke, D. Fournier, L. Belliard, A. Le Febvrier, C. Pallier and P. Eklund, *J. Phys. D Appl. Phys.*, 2018, **51**, 355302.
17 B. Wei, H. Liang, D. Zhang, Z. Wu, Z. Qi and Z. Wang, *J. Mater. Chem. A*, 2017, **5**, 2844–2851.
18 X. Y. Zhang, J. S. Chawla, B. M. Howe and D. Gall, *Phys. Rev. B:condens. Matter Mater. Phys.*, 2011, **83**, 165205.
19 S. Lee, K. Esfarjani, T. Luo, J. Zhou, Z. Tian and G. Chen, *Nat. Commun.*, 2014, **5**, 1–8.
20 M. Novaković, M. Popović, Z. Rakočević and N. Bibić, *Process. Appl. Ceram.*, 2017, **11**, 45–51.
21 A. Garzon-Fontecha, H. A. Castillo, E. Restrepo-Parra and W. De La Cruz, *Surf. Coat. Technol.*, 2018, **334**, 98–104.
22 D. Gall, C. S. Shin, R. T. Haasch, I. Petrov and J. E. Greene, *J. Appl. Phys.*, 2002, **91**, 5882–5886.
23 A. Herwadkar and W. R. L. Lambrecht, *Phys. Rev. B:condens. Matter Mater. Phys.*, 2009, **79**, 035125.
24 G. Kogo, H. Lee, A. H. Ibrahim, X. Bo, S. K. Pradhan and M. Bahoura, *J. Appl. Phys.*, 2018, **124**, 165106.
25 R. Chavez, S. Angst, J. Hall, F. Maculewicz, J. Stoetzel, H. Wiggers, L. Thanh Hung, N. Van Nong, N. Pryds, G. Span, D. E. Wolf, R. Schmechel and G. Schierning, *J. Phys. D Appl. Phys.*, 2017, **51**, 014005.
26 A. Le Febvrier, N. Van Nong, G. Abadias and P. Eklund, *Appl. Phys. Express*, 2018, **11**, 051003.
27 T. Aizawa, F. F. Yun and T. Mori, *ACS Appl. Energy Mater.*, 2025, **8**, 13360–13366.
28 A. Le Febvrier, D. Gambino, F. Giovannelli, B. Bakhit, S. Hurand, G. Abadias, B. Alling and P. Eklund, *Phys. Rev. B*, 2022, **105**, 104108.
29 T. Nakano, K. Hoshi and S. Baba, *Vacuum*, 2008, **83**, 467–469.
30 B. Ravel and M. Newville, *J. Synchrotron Radiat.*, 2005, **12**, 537–541.
31 N. Jiang, D. G. Georgiev and A. H. Jayatissa, *Semicond. Sci. Technol.*, 2013, **28**, 25009–25017.
32 S. Chowdhury, V. Hjort, R. Shu, G. Greczynski, A. Le Febvrier and M. Magnuson, *Phys. Rev. B*, 2051, **108**, 205134.
33 P. Tomeš, D. Logvinovich, J. Hejtmánek, M. H. Aguirre and A. Weidenkaff, *Acta Mater.*, 2011, **59**, 1134–1140.
34 O. Jankovský, D. Sedmidubský, Š. Huber, P. Šimek and Z. Sofer, *J. Eur. Ceram. Soc.*, 2014, **34**, 4131–4136.
35 M. E. McGahay, S. V. Khare and D. Gall, *Phys. Rev. B*, 2020, **102**, 235102.
36 Y. Tripathi, R. Gupta, Seema, M. Gupta, D. M. Phase and P. Rajput, *Thin Solid Films*, 2019, **670**, 113–121.
37 Y. Shuang, S. Mori, T. Yamamoto, S. Hatayama, Y. Saito, P. J. Fons, Y. H. Song, J. P. Hong, D. Ando and Y. Sutou, *ACS Nano*, 2024, **18**, 21135–21143.
38 B. Biswas, S. Chakraborty, O. Chowdhury, D. Rao, A. I. K. Pillai, V. Bhatia, M. Garbrecht, J. P. Feser and B. Saha, *Phys. Rev. Mater.*, 2021, **5**, 114605.
39 B. Alling, T. Marten and I. A. Abrikosov, *Phys. Rev. B*, 2010, **82**, 184430.

